Chapter 2

Detailed numerical simulation of a Multidimensional co-flow partially premixed methane/air laminar flame

Contents of this chapter are published as:
K. Claramunt, R. Cònsul, C.D. Pérez-Segarra, and A. Oliva. Multidimensional mathematical modeling and numerical investigation of co-flow partially premixed methane/air laminar flames. *Combustion and Flame*, 137:444–457, 2004.

Abstract. The goal of this paper is to analyse, by means of detailed numerical simulations, the influence of the partially premixing level and the adequacy of different mathematical sub-models on the modelization of co-flow partially premixed methane-air laminar flames. Five levels of premixing of the primary inlet are considered from an equivalence ratio of $\Phi = \infty$ (non-premixed flame) to $\Phi = 2.464$. Main flame properties are provided giving special emphasis to the analysis of pollutant formation. Different mathematical formulation aspects (several chemical mechanisms, radiation effects, mass transport models and inlet boundary conditions) have been tested and validated against experimental data available in the literature. Finite volume techniques over staggered grids are used to discretize the governing equations. A parallel multiblock algorithm based on domain decomposition techniques running with loosely coupled computers has been used obtaining a competitive ratio between computational cost and resources. To assess the quality of the numerical solutions presented in this paper, a verification process based on the generalised Richardson extrapolation technique and on the Grid Convergence Index (GCI) has been applied.

Keywords:Co-flow methane/air laminar flames, combustion, mathematical formulation analysis, levels of premixing analysis, numerical simulation, verification and validation

2.1 Introduction

In the last decades, comprehensive studies have been reported in the literature concerning detailed experimental and numerical analysis of laminar flames in simple systems. Among them, and due to their wide application in house-hold and industrial heating systems, the analysis of co-flow laminar flames has motivated a special interest. These studies have usually been focused on non-premixed or premixed flames. More recently these studies have been extended to partially premixed situations [1, 2] due to its significant practical and fundamental importance.

Partially premixed flames are formed when less than the stoichiometric amount of oxidizer is mixed in a fuel flow upstream of the reaction zone, in which additional oxidizer is available to diffuse into the flame and provide complete combustion [3]. Due to their stability, partially premixed flames are used in Bunsen burners, furnaces, gas-turbine combustor flames, gas-fired domestic appliances, and other common combustion devices. Recent studies suggest that an optimum operating condition exists which minimises the pollutant emissions, and thus enhances the design of cleaner practical burning combustors.

With the increase of the computational power, the improvement of the numerical methods and the use of more accurate experimental techniques, the knowledge of the combustion phenomenon taking place in these flames has been considerably increased.

Experimental studies have provided measurements of temperature, major species, radicals, nitrogen oxides and soot. Mass spectrometry, Raman and LIF techniques have been employed to study co-flow flames under different geometrical configurations, equivalence ratios, and pressure-conditions [1, 4–6].

Concerning numerical studies, from one of the first multidimensional simulations of co-flow methane-air laminar flames carried out by Mitchell et al [7], a considerable improvement of the accuracy of the mathematical models employed for the simulations has been achieved. Detailed numerical simulations with fully elliptic equations, complex transport formulation and detailed chemistry have been reported. C1 and C2 chemical mechanisms are mainly employed and compared [8], molecular transport is modelized under different assumptions [9], soot formation is sometimes modelled [5], and radiation transfer, if considered, is usually evaluated with simplified models [10].

In spite of the above mentioned progress achieved, there is a certain interest in the combustion community to continue working on the detailed analysis of these simple flames. Although combustion nearly always takes place within turbulent flow fields which increase the mixing process, and thereby enhance combustion [11], deep understanding of laminar combustion is a basic ingredient of the modelization of turbulent flames, as well as of pollutant formation.

The aim of this work is to contribute to this interest by investigating, by means of detailed numerical simulations, the influence of the partially premixing level and the adequacy of different mathematical sub-models, in a co-flow partially premixed

methane-air flame.

The numerical study is performed both analysing main flame features and local data. The amount of pollutant produced is presented by means of the evaluation of emission indexes EI_x, defined as the fraction between grams per second of pollutant species and kilograms per second of methane burned.

Special emphasis is given to assess the quality of the numerical solutions and to reproduce experimental conditions (i.e. verification and validation processes). Numerical solutions are verified using the post-processing procedure described in [12] based on the Generalised Richardson extrapolation technique for h-refinement studies and on the Grid Convergence Index (GCI) proposed by Roache [13]. The validation of the mathematical models is carried out considering the experimental data provided in [2, 6].

A parallel multiblock algorithm [14], specially developed to be used in loosely coupled parallel computers (Beowulf clusters), has been employed to perform the numerical simulations allowing an exhaustive analysis of the flame with an excellent ratio between computational time and resources.

2.2 Problem definition

The flame considered is the co-flow partially premixed methane/air laminar flame with the burner characteristics defined in [2]. Experimental apparatus and measurement techniques are extensively described in [5, 6, 15]. Hereafter, a brief description of the test assay is presented. Figure 2.1 shows a schematic representation of the burner. Fuel mixed with primary air flows from an uncooled $r_i = 5.55$ mm inner radius brass tube with a wall thickness of $w_i = 0.8$ mm. Air is injected from the annular region between this tube and a concentric $r_o = 47.6$ mm inner radius brass cylinder. The outer tube thickness is $w_o = 3.4$ mm. Fuel tube contains a length of 110 mm of glass beads in order to smooth the flow, and to assure a fully developed velocity profile at the exit. A perforated brass plate, glass beads and finally a 1.5 mm cell-size ceramic honeycomb straighten the air flow. The inner tube extends 4 mm above the honeycomb surface to facilitate the access to the lowest flame regions. The cylindrical brass chimney that confines the flame and protects it from laboratory air movements has a diameter of 102 mm.

Different levels of premixing of the primary inlet are considered from an equivalence ratio of $\Phi = \infty$ (non-premixed flame) to $\Phi = 2.464$. The lower limit was just before flashback began to affect the flame structure [15]. Equivalence ratios and mass flows are listed in Table 2.1. Primary air is oxygen-enriched (25% O_2 by volume) and secondary air is "regular" (20.9% O_2). Due to the considerable complexity of the burner configuration below the bottom of the flame (presence of perforated brass plates, glass beads and ceramic honeycomb structures), only the region above the

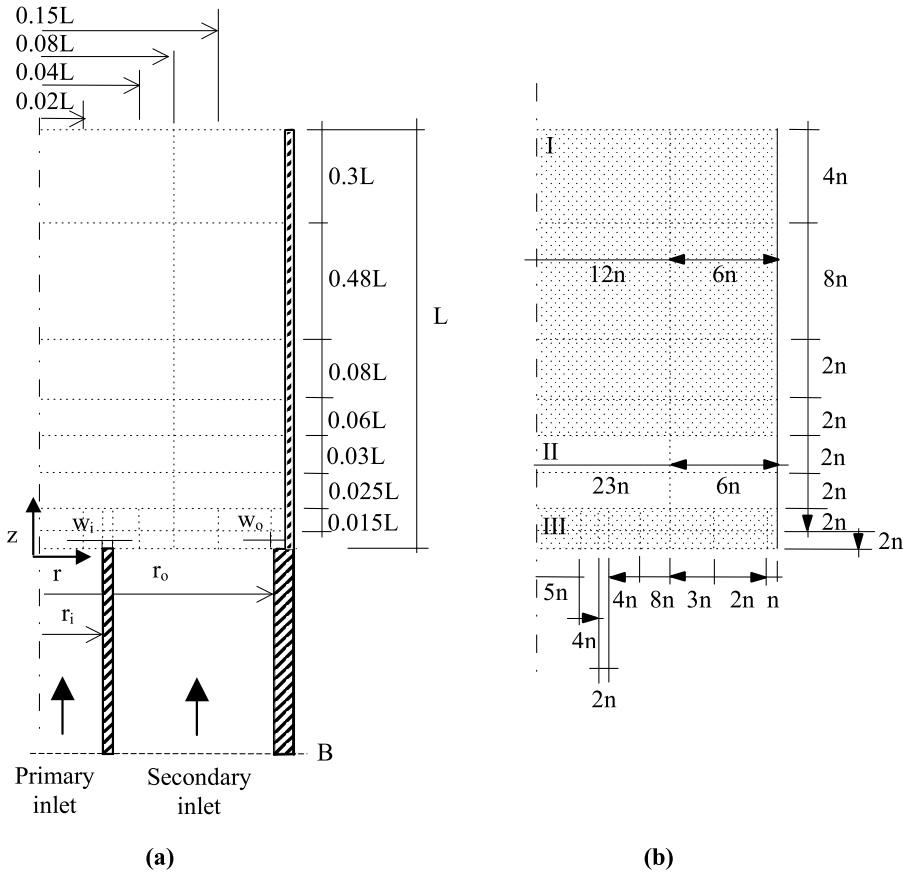

Figure 2.1: Confined co-flow methane/air laminar flame. (a) Burner idealized geometry and definition of the different zones for the non-equispaced cylindrical grid. (b) Definition of macro zones (I, II and III) and their mesh nodes distribution (solid triangles indicate the direction of grid nodes intensification).

Φ	$\dot{m}_{CH_4}$ (g/min)	$\dot{m}_{air}$ (g/min)
Inner jet		
∞	0.2165	0.0000
12.320	0.2165	0.2493
6.160	0.2165	0.4986
4.107	0.2165	0.7478
2.464	0.2165	1.2465
Outer jet		
All	0.0000	51.879

Table 2.1: Flame parameters.

inner tube exit has been simulated (i.e. $z > 0$). A computational height of $L = 200$ mm has been considered according to numerical results presented in [2]. See Fig. 2.1 for details.

2.3 Mathematical model

The fluid flow, and heat and mass transfer phenomena of the reactive gas in the co-flow partially premixed methane-air laminar flame defined above is assumed to be described by the governing equations for low-Mach number flows (continuity, species, momentum, energy and state equation) [14].

A modelization of the chemical mechanisms, molecular transport fluxes and radiation heat flux is required to close the problem. Furthermore, special attention has to be paid to boundary conditions. Thermo-physical properties are evaluated using the thermodynamic data compiled in [16].

2.3.1 Mathematical sub-models

The detailed chemical mechanism considered is the GRI-Mech 3.0 [16] which involves 325 reactions and 53 species. This mechanism is suitable for the description of pollutant formation because it includes NO_x reactions.

The shear stress tensor ($\vec{\tau}$) is evaluated taking into account Stokes' law for Newtonian fluids considering a mixture viscosity. Diffusion heat flux ($\vec{q}$) considers Fourier's conduction and the energy transport by inter-diffusion. Mass fluxes of species are evaluated considering both an equivalent Fickian diffusion and thermal diffusion (Soret effect) term [17]:

$$\vec{j_i} = -\rho \mathcal{D}_{im} \nabla Y_i - D_i^T \nabla \ln T \tag{2.1}$$

where, $\mathcal{D}_{im}$ and D_i^T are the multicomponent ordinary and thermal diffusion coefficients respectively.

Transport coefficients of the molecular fluxes of momentum $\vec{\tau}$, heat $\vec{q}$ and mass $\vec{j_i}$ are evaluated considering a mixture-averaged formulation. Pure-species transport properties are evaluated using CHEMKIN's database [18]. For the mixture-averaged viscosity and the thermal conductivity, the semi-empirical Wilke (1950) formulae, modified by Bird (1960) is used [17]. Mixture diffusion coefficients $\mathcal{D}_{im}$, which appear in Eq. 2.1, are calculated from the *Stefan-Maxwell* equation and considering *trace-species* approximation [17]. Assuming that a given species sees the rest moving with the same average velocity, and when the mixture is composed by one majority species, the equivalent Fickian diffusion coefficient of one species into the mixture can be formulated with $\mathcal{D}_{im} = (1 - Y_i)/\tilde{X}$ where $\tilde{X} = \sum_{j=1,j\neq i}^{N} X_j/\mathcal{D}_{ij}$ and $\mathcal{D}_{ij}$ represents the binary diffusion coefficient [17]. Thermal diffusion coefficients D_i^T are obtained relating calculated $\mathcal{D}_{im}$ values with the thermal diffusion ratios (see [18]).

Flame radiation is modelled using the assumption of optically thin transfer between the hot combustion gases and the cold surroundings [19, 20]. The definition of an optically thin gas establishes that self-absorption is negligible compared to emission. A term for the absorption of radiation coming from the surrounding background at T_s temperature is included. When T_s is low, this term can be neglected. Thus, the radiative heat loss term per unit of volume is expressed as:

$$\nabla \cdot \vec{q}^{\,R} = 4\sigma T^4 \sum_{i=1}^{N} (p_i \kappa_{P_i}) - 4\sigma T_s^4 \sum_{i=1}^{N} (p_i \kappa_{I_i}) \tag{2.2}$$

where σ is Stefan-Boltzmann constant; p_i is the partial pressure of species i; κ_{P_i} is the Planck-mean absorption coefficient for species i; κ_{I_i} is the incident-mean absorption coefficient for species i; T_s is the background temperature.

The radiating species considered in order of importance are CO_2, H_2O, CH_4 and CO. From running RADCAL [21], Planck-mean and incident-mean absorption coefficients, which are fitted to polynomial expressions [19], are obtained at different temperatures.

2.3.2 Boundary conditions

Special attention has been paid to the inlet boundary conditions at $z = 0$ in order to relate their values with the known values at the bottom of the burner (section B in Fig. 2.1a). Species mass fractions are evaluated fixing species mass flow rates and considering that no reaction occurs inside the tube:

$$(\rho v_z Y_i)_B = \left[\rho v_z Y_i - \rho D_{im} \frac{\partial Y_i}{\partial z} - D_{im}^T \frac{\partial \ln T}{\partial z} \right]_{z=0} \tag{2.3}$$

For the energy equation, in preceding works [2, 10], an ambient under-predicted ($298K$) temperature was fixed at the entrance of the computational domain ($z = 0$). In this work, an enthalpy flux is evaluated at section B and, assuming a temperature at section B of $T_B = 298K$, the temperature is estimated solving Eq. 2.4. This boundary condition implies that no heat flux is transferred through the inner tube between the primary and secondary fluxes.

$$(\rho v_z h)_B = \left[\rho v_z h - \lambda \frac{\partial T}{\partial z} - \sum_{i=1}^{N} h_i \left(\rho D_{im} \frac{\partial Y_i}{\partial z} + D_{im}^T \frac{\partial \ln T}{\partial z} \right) \right]_{z=0} \tag{2.4}$$

Due to the configuration of the burner, the radial component of the velocity has been neglected at the entrance of the computational domain ($z = 0$) of both primary and secondary flows. In order to take into account the considerable gradients of temperature and mass fractions involved in the inlet region, axial velocity is calculated using the local density value and assuming a mass flow rate profile: a parabolic mass flow rate for the primary inlet and a plug-flow profile for the secondary one.

The chimney has been considered to be impermeable and chemically inert (material without any chemical activity), being the total flux of species normal to the wall equal to zero. At the outlet of the burner, a pressure outflow boundary condition is imposed [22], and a null gradient in the axial direction of temperature and species is assumed.

2.4 Numerical Methodology

The mathematical model is discretized using the finite volume technique over cylindrical staggered grids. Central differences are employed for the evaluation of the diffusion terms, while third-order bounded schemes are used for the evaluation of the convective ones [23]. A time-marching SIMPLE-like algorithm is employed to couple velocity-pressure fields. Discretized equations are solved in a segregated manner [24] using a multigrid solver [25]. The convergence of the time-marching iterative procedure is truncated once normalised residuals are below 10^{-8}.

On the resolution of species equations, and in order to overcome the stiffness of the governing equations, a pseudo-time splitting technique is used [14]. Energy equation is considered in terms of enthalpy transport. Instead of solving this equation directly, a temperature convection-diffusion equation is considered, and the full enthalpy transport equation is introduced in the source term by means of a deferred correction (see [14] for details).

The computational domain has been discretized using a cylindrical structured grid. Several zones with different grid nodes distributions are defined (Fig. 2.1b). The number of grid nodes is increased at the outlet of the inner tube where the

gradients of methane are higher. As we move away from the bottom and from the flame front, the grid nodes density is progressively decreased by means of tanh-like functions. The number of nodes corresponding to each zone is indicated in terms of the grid parameter n, and the direction of the intensified distribution is indicated by a solid triangle.

Domain decomposition method is used as a strategy to reduce the number of grid nodes far from the flame fronts, and as a parallelisation technique. The whole domain is divided into several overlapped *subdomains* joined by the interpolation boundaries [14, 26]. Each CPU solve one (or a group) of subdomains, and only one communication for each outer iteration is required. This is an important feature when *Beowulf* clusters are used. For further details see [14, 26, 27].

Due to the parabolic structure of the flow, the domain is decomposed in eight subdomains in z-direction. The computational behaviour of the parallel multiblock algorithm confirms this strategy. The use of the multiblock discretization allows the definition of 3 macro zones, identified in the figure with Roman numbers, characterised by having the same grid-nodes distribution in r-direction.

All the numerical simulations have been performed on a *Beowulf cluster* composed by 48 standard PCs (AMD K7 CPU at 900 MHz and 512 Mbytes) with a conventional network.

2.5 Verification and validation processes

2.5.1 Verification procedure and results

A post-processing procedure [12], based on the generalised Richardson extrapolation for h-refinement studies and on the Grid Convergence Index (GCI) proposed by Roache [13], has been used in order to establish a criteria on the sensitivity of the simulation to the computational model parameters that account for the discretization: the mesh spacing and the order of accuracy. This tool estimates the order of accuracy of the numerical solution (observed order of accuracy p), and the error band where the grid independent solution is expected to be contained (uncertainty due to discretization GCI), also giving criteria on the credibility of these estimations. See [12, 14] for further details about this post-processing procedure.

Local estimators of the GCI and p are calculated at the grid nodes where monotone convergence is observed. These grid nodes are named Richardson nodes Rn. Global values of GCI and p are calculated by means of volumetric and arithmetic averaging respectively. It is considered that an estimation is credible when the global observed order of accuracy p approaches the theoretical value, and when the number of Richardson nodes is high enough. See [12] for details.

The h-refinement study is performed with five levels of refinement ($n = 1, 2, 4, 8$

$\Phi = \infty$									
grid						GCI^* [%]			
n	$T_{max,C}$	Hf	EI_{CO}	EI_{NO}	EI_{NO_2}	$T^* = T/298$	Y_{CO}	Y_{NO}	Y_{NO_2}
4	1908.37	5.860	0.331	3.181	0.450	$3.4\text{x}10^{-1}$	$4.4\text{x}10^{-4}$	$9.2\text{x}10^{-5}$	$2.6\text{x}10^{-6}$
8	1908.56	5.852	0.323	3.224	0.452	$6.0\text{x}10^{-2}$	$1.0\text{x}10^{-4}$	$1.6\text{x}10^{-5}$	$1.2\text{x}10^{-6}$
16	1908.51	5.838	0.321	3.248	0.452	$9.4\text{x}10^{-3}$	$3.9\text{x}10^{-5}$	$6.0\text{x}10^{-6}$	$5.2\text{x}10^{-7}$
$\Phi = 2.464$									
grid						GCI^* [%]			
n	$T_{max,C}$	Hf	EI_{CO}	EI_{NO}	EI_{NO_2}	$T^* = T/298$	Y_{CO}	Y_{NO}	Y_{NO_2}
4	2032.55	4.012	0.225	2.692	0.372	$1.6\text{x}10^{-1}$	$4.7\text{x}10^{-4}$	$6.2\text{x}10^{-6}$	$1.4\text{x}10^{-6}$
8	2033.59	3.985	0.217	2.699	0.366	$3.1\text{x}10^{-2}$	$2.6\text{x}10^{-4}$	$1.7\text{x}10^{-6}$	$2.4\text{x}10^{-6}$
16	2033.65	3.982	0.216	2.700	0.365	$7.7\text{x}10^{-3}$	$2.8\text{x}10^{-5}$	$2.7\text{x}10^{-7}$	$2.9\text{x}10^{-7}$

Table 2.2: Verification of the numerical solutions. Main flame features. (Φ: equivalence ratio; n: grid parameter; $T_{max,C}$: maximum temperature at the symmetry axis; Hf: flame height; EI_x: emission index). Post-processing results. (For table description see section 2.5.).

and 16). For example, for the finest discretization $n = 16$, 141.856 CVs are employed. Estimations are given for a zone limited by $0 \leq r \leq 1.59\ cm$ and $0 \leq z \leq 20\ cm$, which is in fact the space region that encloses the flame.

In Table 2.2, the main flame features, together with the uncertainty estimates for temperature and mass fractions of CO, NO and NO_2, are given for the last three highest levels of refinement ($n = 4, 8$ and 16) and both extreme cases of premixing (i.e. $\Phi = \infty$ and $\Phi = 2.464$). An asymptotic convergence behaviour of the maximum temperature at the centerline, the height of the flame and the emission indexes of CO, NO and NO_2 is observed. GCI values for the third level of refinement ($n = 4$) already reach an adequate level of accuracy. For instance, non-dimensional temperature has an average uncertainty of $\pm 0.34\%$ (i.e. approximately $\pm 1K$ for its dimensional value). These estimations agrees with the asymptotically behaviour of mean flame properties.

The percentage of Richardson nodes (Rn) of the numerical solutions presented in this paper has been found to be sufficiently large for all the variables (i.e. in general higher than 75%). When the grid is refined, the number of Richardson nodes increases, and uncertainty estimates reduce their value approximately by four, as expected. Furthermore, the global order of accuracy (p) for each variable agree with its theoretical value.

Computational costs, in terms of CPU seconds per outer iteration, for the above mentioned three levels of refinements are 11.12, 38.57 and 146.1 respectively [14].

Φ	$T_{max,C}$ $[K]$	Hf $[cm]$	T_{max} $[K]$	(r,z) $[mm]$	RHL $[W]$	HR $[W]$	EI_{CO} $[g/kg]$	EI_{NO} $[g/kg)$	EI_{NO_2} $[g/kg)$
∞	1908 (1960)	5.9 (5.7)	2005	0.66, 0.66	35.11	181.05	0.33	3.2	0.45
12.32	1933 (2000)	5.6 (5.2)	2009	0.65, 0.72	34.83	180.99	0.30	3.2	0.46
6.160	1956 (2020)	5.2 (4.9)	2017	0.63, 0.97	34.75	180.91	0.28	3.1	0.43
4.107	1980 (2040)	4.8 (4.5)	2031	0.61, 1.41	34.79	180.74	0.26	3.0	0.41
2.464	2033 (2090)	4.0 (3.8)	2083	0.57, 1.97	35.04	180.35	0.22	2.7	0.37

Table 2.3: Main flame characteristics for the different levels of premixing. (Φ: equivalence ratio; $T_{max,C}$: maximum temperature at the symmetry axis; Hf: flame height; $T_{max}, (r,z)$: maximum flame temperature and location; RHL radiant heat loss; RH: heat release; EI_x: emission index). Experimental results [2] are in parenthesis.

Approximately 3000 outer iterations are needed to reach a highly converged solution (normalised residuals below 10^{-8}). According to these computational costs and the obtained uncertainty estimates, the third level of refinement ($n = 4$) has been considered the most appropriate to perform the numerical studies hereafter presented, both in terms of accuracy (numerical credibility) and computational time.

2.5.2 Validation

The numerical simulation results are compared with experimental data [2]. The conclusions on the agreement to experimental data should be carefully considered due to the measurements uncertainties described in [2]. Table 2.3 shows the main flame characteristics for all levels of partially premixing. The flame height decreases whilst the partially premixing level increases The amount of oxygen introduced through the primary inlet reduces the axial distance that it has to overcome to diffuse into the flame and to create stoichiometric conditions. Flame height predictions are in good agreement with experimental results (discrepancies are always lower than 7%). In all cases an over-prediction is obtained.

Computational temperatures also show good agreement to experimental data. Maximum centerline temperatures disagree less than 3.4% for all premixing cases. General trends observed in experimental studies are appropriately reproduced in the numerical results. Figure 2.2 shows the temperature profiles along the centerline for the different equivalence ratios. As can be seen, as equivalence ratio decreases, temperature increases and profiles present sharper gradients.

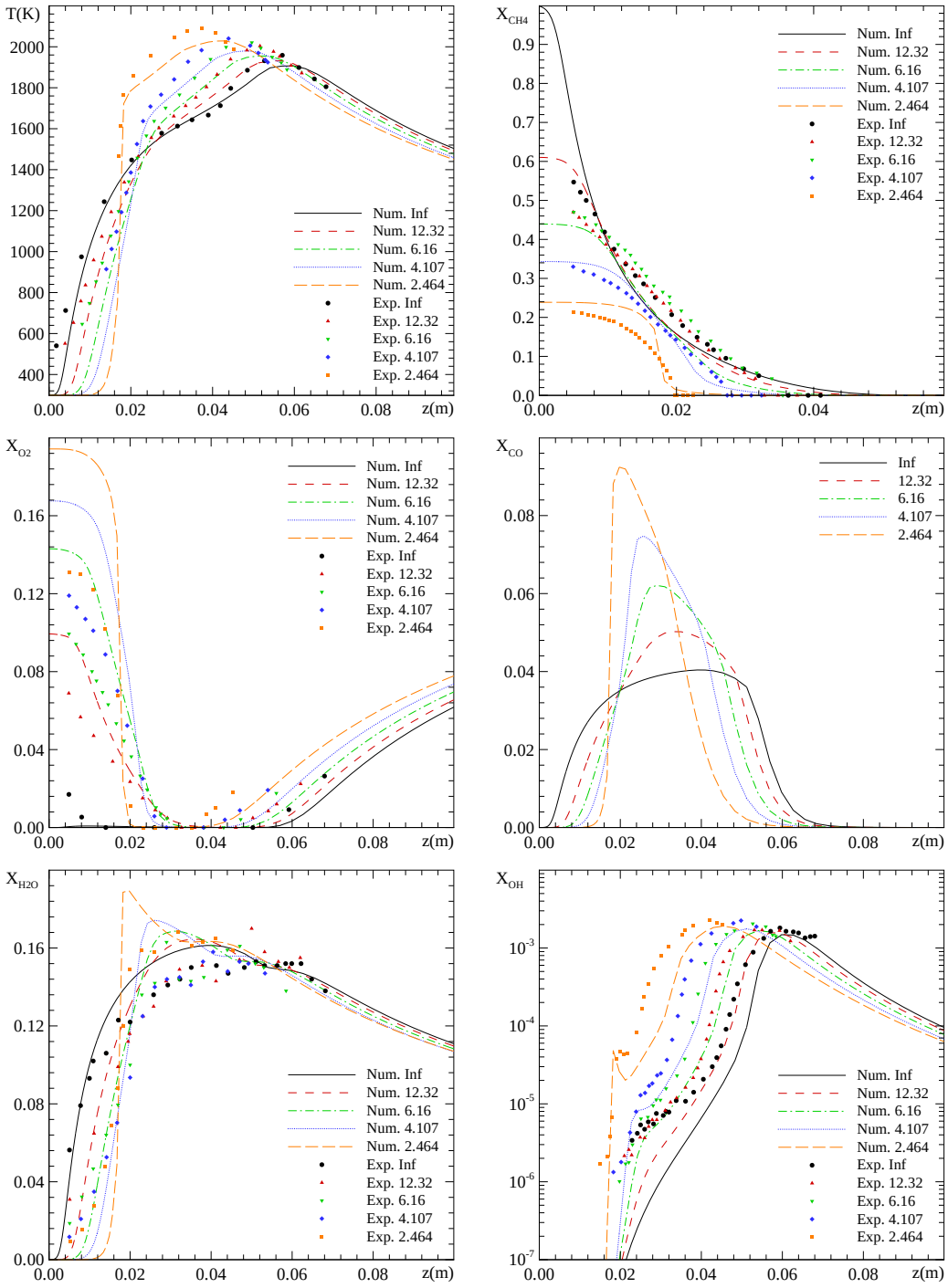

Figure 2.2: Comparison of numerical results (lines) vs. experimental data (dots) by [2] along the symmetry axis.

Well-known temperature maps are obtained for the non-premixed situation, whilst for the flame with equivalence ratio $\Phi = 2.464$, the structure of non-premixed and premixed flames are mixed, forming what is known as a *double flame*. The outer flame region clearly has a non-premixed structure, whilst the inner region defines a classical premixed shape. In the non-premixed situation, a larger amount of fresh air (from the secondary inlet) enters the flame, decreasing temperature maps.

Major species centerline profiles are also plotted in Fig. 2.2. Although significant disagreements have been obtained between numerical and experimental data, global trends of the influence of the premixing level are well predicted.

Results for the non-premixed flame show the well-known diffusion flame structure. Maximum CH_4 mole fractions are held at the axis, while O_2 and N_2 surround the flame. Combustion products are formed near the stoichiometric surface. Fuel decomposes forming H_2, CO and H_2O on the rich side of the flame front. CO oxidises forming CO_2 mainly at the top of the flame. As the level of premixing increases, the reactants (CH_4 and O_2) need further time before they start to react. The higher injection velocities produce relatively flat profiles at the inner tube exit. Sharper gradients are also predicted.

The double flame structure effects can also be observed in the H_2O mole fractions profiles presented in Fig. 2.2 for $\Phi = 2.464$. The presence of a marked peak followed by a second smaller one denotes two main zones of H_2O production. At the first flame front, with premixing features, the mole fraction peak increases with the level of premixing. H_2O measurements present a more aleatory behaviour (experimental calibration difficulties for H_2O mole fractions due to the low vapour pressure conditions are reported in [2]). However, both computational and experimental results coincide with the fact that the greatest amount of H_2O is produced at the inner flame front, and with the observation of an inner peak for the higher premixing conditions.

OH mole fractions are also given in Fig. 2.2. General trends coincide for both computational and experimental profiles. Once again, the double flame structure for the highest levels of premixing is predicted by the presence of an inner peak. In this case the amount of OH formed in the inner flame is considerably lower than the one produced in the outer one.

2.6 Discussion

2.6.1 Pollutant formation

One of the most relevant aspects in the analysis of co-flow methane/air flames are the studies of pollutant formation and the influence of the equivalence ratio in partially premixed flames. Global trends of NO_x emission predicted by GRI-Mech 3.0 are given in Table 2.3. As can be seen, similar amounts of NO and NO_2 are predicted

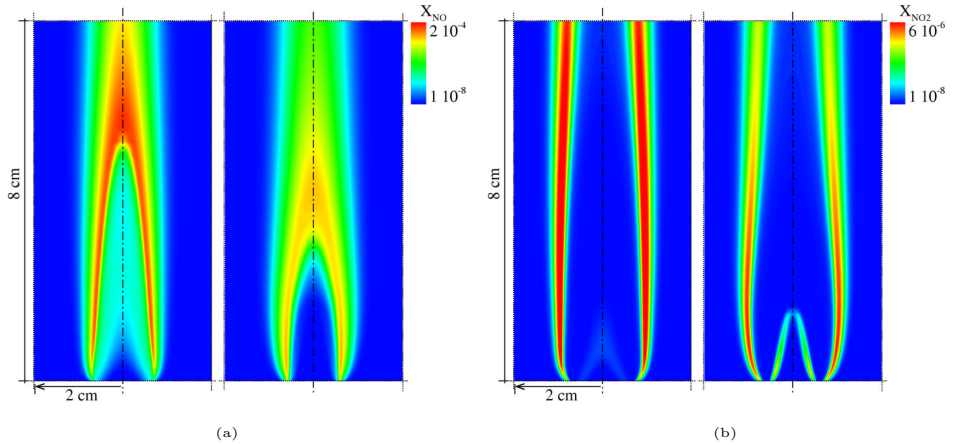

Figure 2.3: Pollutant formation. Mole fractions isopleths for: nitrogen oxide, NO (top); nitrogen dioxide, NO_2 (bottom). Two premixing levels: $\Phi = \infty$ (left); $\Phi = 2.464$ (right).

for equivalence ratios between $\Phi = 4.107$ and $\Phi = \infty$. When the premixing level increases, the higher production of thermal NO is balanced by a reduction of prompt NO [28]. Although the residence time reduces when the level of partial premixing increases, the higher temperatures achieved between inner and outer flames increases the amount of NO_x produced. For lower values of Φ a reduction of NO_x is predicted. Similar trends were observed by Gore et al [28] in their experimental measurements. They suggested that these reduction could be associated to the reduction of prompt NO caused by intermediate hydrocarbon chemistry and contributions from the reverse prompt mechanism described by Takagi and Xu [29]. Isopleths for NO and NO_2 are plotted in Fig. 2.3. Higher NO_x emissions are observed qualitatively for the non-premixed flame (left figures). A larger amount of prompt NO formed mainly at the stoichiometric surface is predicted for the non-premixed flame. NO_2 contours show the double flame structure for $\Phi = 2.464$. Although CO mole fraction experimental measurements are not provided in [2], computational results are also given to show the premixing dependence of its production (Fig. 2.2). As can be seen, for the non-premixed flame, CO production does not present a remarkable peak. It is progressively produced in the inner flame region. At the top of the flame it is partially consumed to produce CO_2. As the level of premixing increases, the CO peak becomes slender. O_2 injected through the primary inlet does not reduce CO concentration, since CO is mainly oxidised by reactions involving OH radical. At the inner premixed

flame front, a considerable amount of CO is produced. At the inner diffusion flame, carbon monoxide is progressively consumed.

CO emission indexes are also given in Table 2.3. CO emissions are small in comparison with NO. An increase of about 10% is predicted from $\Phi = 12.32$ to $\Phi = \infty$. These differences increase notably when the highest level of premixing is considered, reducing CO emission index to about 33%. This tendency confirms the experimental results presented in [28].

2.6.2 Mathematical sub-models analysis

The adequacy of different mathematical sub-models is presented here. For comparison purposes, the mathematical model described in section 2.3 is referred to as the *reference model*.

A summary of these studies is presented in Table 2.4 for the extreme premixing situations ($\Phi = \infty$ and $\Phi = 2.464$) . Maximum temperature at the centerline, flame height, maximum flame temperature and its location and emission indexes for CO, NO and NO_2 are shown in this table for all modelizations tested. The comparison is performed in such a way that the *reference model* criteria are always applied except the model alternative under analysis. The results obtained are given below.

Energy boundary condition

The energy boundary condition used in the *reference model* (Eq. 2.4) is compared with a simple condition, which consists of fixing an ambient temperature of $298K$ at $z = 0$. The influence of both treatments can be observed in Table 2.4 and Fig. 2.4. As expected, when the inlet temperature is fixed, lower maximum temperatures are predicted. The temperature profile along the symmetry axis for both flames ($\Phi = \infty$ and $\Phi = 2.464$) is plotted. There is a better agreement with experimental data when the *reference model* is applied. Temperature profiles for both flames tend to move towards the right, also increasing the maximum temperature at the centerline. Furthermore, emission indexes of pollutant (see Table 2.4) are significantly affected for the energy boundary condition, specially the NO formation which is under-predicted a 18% for $\Phi = \infty$ and a 28% for $\Phi = 2.464$.

Chemical models

Numerical results obtained employing GRI-Mech 3.0 are compared to those obtained with its previous releases (1.2, 2.11) [30], and to a 42-step mechanism (hereinafter referred to as 42-Step-Mech) [31]. The simple irreversible single-step flame-sheet approach [7] is also included giving an idea of its accuracy.

$\Phi = \infty$								
Approach	*Model alternatives*	$T_{max,C}$ $[K]$	Hf $[cm]$	T_{max} $[K]$	(r,z) $[cm]$	EI_{CO} $[g/kg]$	EI_{NO} $[g/kg]$	EI_{NO_2} $[g/kg]$
Experimental [2]		1960	5.7	$--$	$--,--$	$--$	$--$	$--$
Ref. model		1908	5.9	2005	$0.66, 0.66$	0.33	3.2	0.45
Boundary	*Tfixed*	1885	6.1	1968	$0.61, 1.19$	0.37	2.7	0.43
Chemistry	*GRI-Mech* 2.11	1904	5.7	2000	$0.65, 0.78$	0.35	1.6	0.21
	GRI-Mech 1.2	1905	5.7	2002	$0.66, 0.59$	0.37	$--$	$--$
	42-*Step-Mech*	1900	5.6	2025	$0.66, 0.66$	0.66	$--$	$--$
	Flame-Sheet	1971	6.6	2244	$0.64, 0.00$	$--$	$--$	$--$
Radiation	*No-Radiation*	2106	5.7	2106	$0.00, 5.69$	0.19	4.4	0.42
Transport	*Lefixed*	1891	5.9	2001	$0.65, 0.78$	0.33	3.2	0.46
	Leunity	1997	6.1	2042	$0.67, 0.48$	0.44	4.0	0.45
	No-Soret	1910	5.9	2013	$0.66, 0.66$	0.32	3.2	0.41

$\Phi = 2.464$								
Approach	*Model alternatives*	$T_{max,C}$ $[K]$	Hf $[cm]$	T_{max} $[K]$	(r,z) $[cm]$	EI_{CO} $[g/kg]$	EI_{NO} $[g/kg]$	EI_{NO_2} $[g/kg]$
Experimental [2]		2090	3.8	$--$	$--,--$	$--$	$--$	$--$
Ref. model		2033	4.0	2083	$0.57, 1.97$	0.22	2.7	0.37
Boundary	*Tfixed*	2005	4.2	2047	$0.54, 2.42$	0.26	2.1	0.34
Chemistry	*GRI-Mech* 2.11	2029	3.9	2068	$0.54, 2.12$	0.24	2.0	0.23
	GRI-Mech 1.2	2030	3.9	2068	$0.54, 2.12$	0.26	$--$	$--$
	42-*Step-Mech*	2024	3.9	2085	$0.59, 0.84$	0.46	$--$	$--$
Radiation	*No-Radiation*	2212	4.0	2211	$0.00, 3.90$	0.14	4.1	0.39
Transport	*Lefixed*	2016	4.0	2078	$0.63, 1.34$	0.22	2.7	0.36
	Leunity	2120	4.3	2139	$0.63, 0.84$	0.29	3.7	0.38
	No-Soret	2033	4.0	2084	$0.63, 1.26$	0.22	2.8	0.35

Table 2.4: Mathematical sub-models analysis. Main flame characteristics. (Φ: equivalence ratio; $T_{max,C}$: maximum temperature at the symmetry axis; Hf: flame height; $T_{max}, (r,z)$: maximum flame temperature and location; EI_x: emission index).

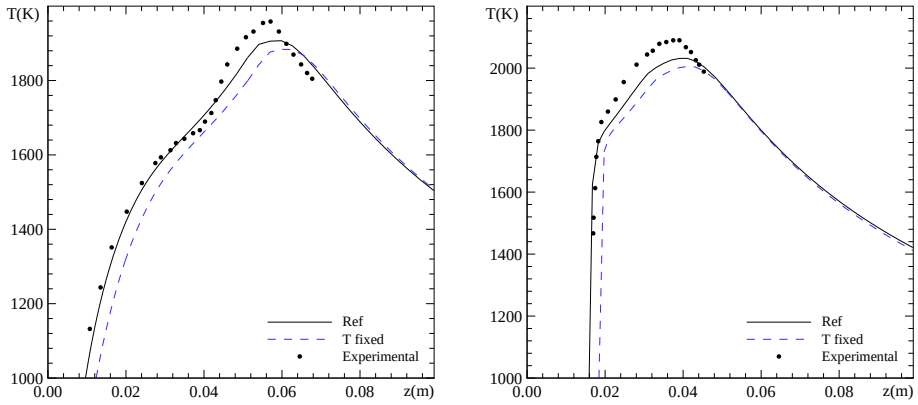

Figure 2.4: Mathematical sub-models analysis. Temperature profiles along the symmetry axis. Energy equation boundary conditions comparison: *Reference model* (solid line) vs. fixed temperature boundary condition (dashed line). Top: $\Phi = \infty$; Bottom: $\Phi = 2.464$. Experimental results in [2].

In a general way, on the prediction of main flame features (see Table 2.4), there is a certain agreement for all mechanisms employed (without considering flame-sheet approach). The most unfavourable comparison with the *reference model* is for 42-Step-Mech that predicts a temperature at the centerline 0.5% lower ($\Phi = 2.464$), and a flame height 5.4% also lower ($\Phi = \infty$). These differences decrease when GRI-Mechs 2.11 and 1.2 are employed. Disagreements about 0.2% and 3.5% for temperature at the centerline and the flame height respectively, are obtained in the most unfavourable situations compared with the *reference model*.

GRI-Mech 2.11 and 1.2 contain the same reactions except the reactions involved in the prediction of NO_x, that are added in 2.11. Thus, very similar results for main flame characteristics are obtained. In centerline and radial profiles (Figs. 2.5-2.7), GRI-Mech 1.2 is not plotted due to its visual fitting with GRI-Mech 2.11 results. This agreement suggests the consideration of NO_x mechanisms in a post-processing procedure (see [32]). Higher differences appear when emission indexes are evaluated. 42-Step-Mech clearly over-predicts CO formation (approximately 100%), while GRI-Mech 2.11 and 1.2 present disagreements of about 10%. Related to NO_x formation, GRI-Mech 3.0 predicts a higher production of these species. This fact is specially important in non-premixed condition (approximately 50%).

Radial profiles of NO and NO_2 mole fractions (Figs. 2.6 and 2.7) emphasise

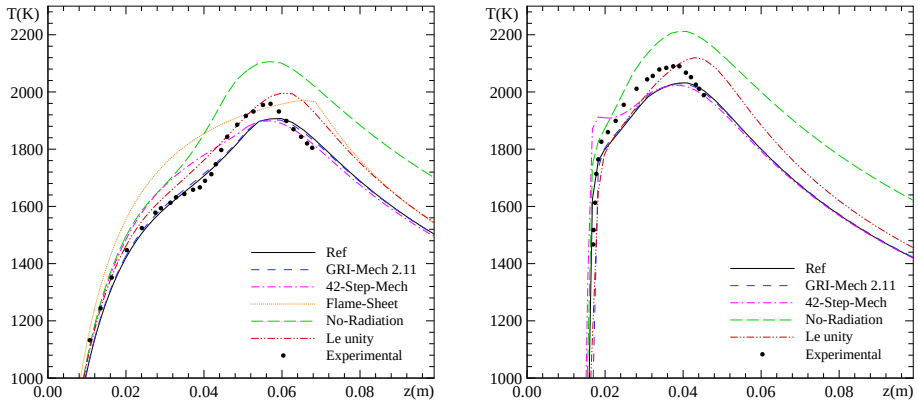

Figure 2.5: Mathematical sub-models analysis. Temperature profiles along the symmetry axis. Top: $\Phi = \infty$; Bottom: $\Phi = 2.464$. Experimental results in [2]. There are no visual differences between GRI-Mechs 2.11 vs. 1.2, and the *reference model* vs. the No-Soret model.

the above mentioned disagreements between 3.0 and 2.11 GRI-Mech releases. As previously commented, version 2.11 under-predicts nitrogen oxides production. The differences obtained for these species are the most important ones in the mathematical approaches comparison.

Radiation

When the radiation model is not considered, important differences as to the *reference model* are observed. For the maximum temperatures at the centerline, differences of nearly 200K for $\Phi = \infty$ flame and approximately 180K for $\Phi = 2.464$ flame are obtained (see Table 2.4). These temperature over-predictions are maintained along the centerline, except at the inner tube exit, where both profiles concur (see Fig. 2.5).

The distributions of CO_2 and H_2O mole fractions have a similar trend (Figs. 2.8 and 2.9). In fact, main differences between both modelizations appear when local radiative heat loss is important. At the inner tube exit and for low enough temperatures, the influence of radiant heat source in energy equation is negligible. When this term increases in importance, local temperature is clearly affected, decreasing its magnitude notably. Referring to nitrogen oxides, important differences are also predicted. In general, neglecting the radiative heat loss implies an over-prediction of NO formation with a factor of two, what is in concordance with the results of Barlow et al

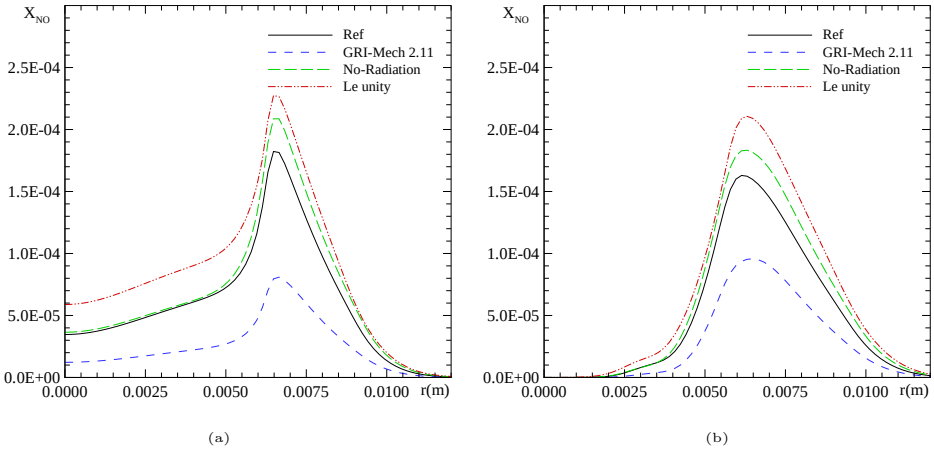

Figure 2.6: Mathematical sub-models analysis. NO mole fraction radial profiles at the axial position of 10 mm. Top: $\Phi = \infty$; Bottom: $\Phi = 2.464$. See Fig. 2.5 for further explanation.

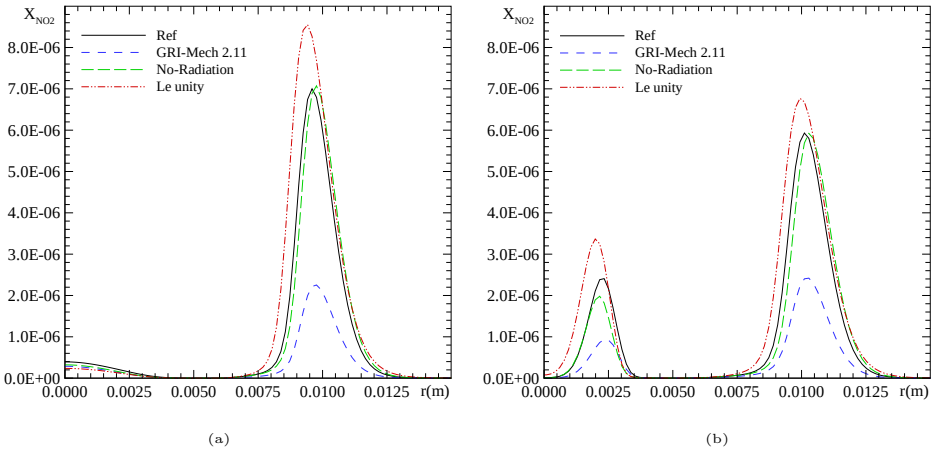

Figure 2.7: Mathematical sub-models analysis. NO_2 mole fraction radial profiles at the axial position of 10 mm. Top: $\Phi = \infty$; Bottom: $\Phi = 2.464$. See Fig. 2.5 for further explanation.

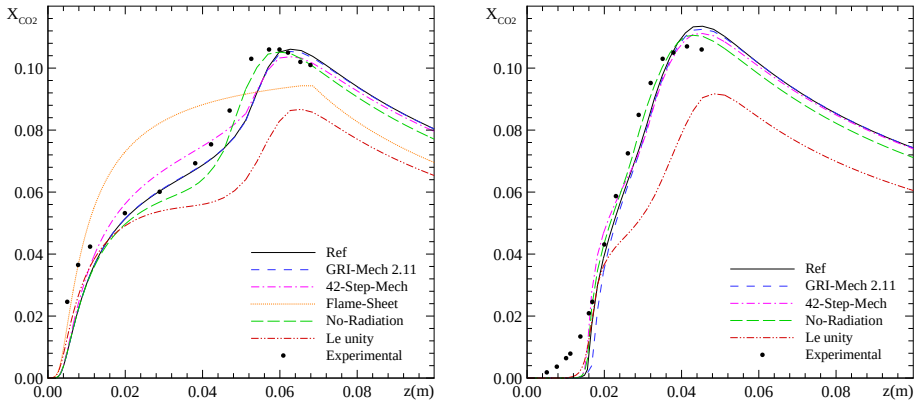

Figure 2.8: Mathematical sub-models analysis. CO_2 mole fraction profiles along the symmetry axis. Top: $\Phi = \infty$; Bottom: $\Phi = 2.464$. Experimental results in [2]. See Fig. 2.5 for further explanation.

(2001) [19]. In fact, and being *thermal* NO_x one of the major contributions to NO_x formation, an increase of temperature consequently supposes an increase of NO_x due to the great temperature dependence of these mechanisms. For NO_2 predictions, the level of the peak with and without the consideration of radiation model is similar (Table 2.4), but a delay on this peak formation is revealed (Fig. 2.7). Most NO_2 is formed at the flame front and it is basically attributed to a *prompt* production. NO_2 radial profile at the base of the flame ($z = 10\ mm$) for the maximum level of premixing considered in this work (i.e. $\Phi = 2.464$), shows the double flame structure characteristic of partially premixed flames.

Mass transport coefficients

The *reference model* calculation of mixture diffusion coefficients $\mathcal{D}_{im}$ is compared with two other possibilities based on the definition of the Lewis number $Le_i = \lambda/(\rho \mathcal{D}_{im} c_p)$:

- Assuming a fixed Lewis number for each species, for instance: $Le_{CH_4} = 0.97$, $Le_{O_2} = 1.11$, $Le_{H_2} = 0.3$. For major species, these fixed Lewis number are provided in the literature (e.g. see [33]). In this work, when fixed Lewis numbers are not provided, they have been evaluated by averaging the local Lewis values obtained from the numerical results performed using the *reference model* (e.g. $Le_{NO} = 1.09$, $Le_{NO_2} = 1.25$, $Le_{N_2O} = 1.39$, $Le_{CN} = 1.09$, $Le_{CH_2CO} = 1.56$,

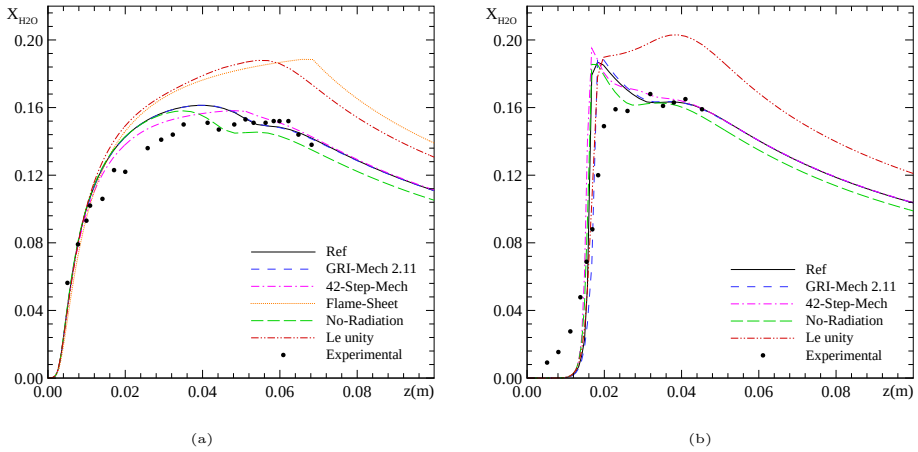

Figure 2.9: Mathematical sub-models analysis. H_2O mole fraction profiles along the symmetry axis. Top: $\Phi = \infty$; Bottom: $\Phi = 2.464$. Experimental results in [2]. See Fig. 2.5 for further explanation.

$Le_{CH_2OH} = 1.35$).

- Assuming a unity Lewis number for all the species involved in the chemical model ($Le_i = 1.0$, $i = 1, 2, ...N$).

Both approximations are commonly used, for example, for the flamelet approach [34, 35], which is a technique usually applied to model turbulent flames. Thus, the interest of the knowledge of the accuracy of these approximations is for both the CPU savings encountered and for a proper application of the mentioned flamelet approach.

Excellent agreement for global and detailed flame properties is achieved (see Table 2.4) when fixed Lewis numbers are used, being the computational effort less intensive in comparison with the complete mixture averaged formulation employed in the *reference model*. CPU time savings of about 25% are obtained.

On the other hand, when a unity Lewis number is considered (second approach), considerable disagreements occur. The maximum temperature at the centerline and the flame height are over-predicted for both extreme levels of premixing (see Table 2.4). CO_2 and H_2O mass fraction profiles present relevant deviations to experimental measurements (Figs. 2.8 and 2.9).

Observing the emission indexes, EI_{CO} is over-predicted as to the *reference model*. Differences of about 33% for $\Phi = \infty$, and 30% for $\Phi = 2.464$ have been observed. Even EI_{NO_2} does not vary significantly, EI_{NO} is also over-predicted with 25% for

$\Phi = \infty$ and 39% for $\Phi = 2.464$. Radial profiles of NO show an over-prediction of this pollutant formation (Fig. 2.6), while profiles of NO_2 are not so dissimilar (Fig. 2.7).

Thermal diffusion ratios are only important for chemical species with mass weights lower than 5 g/mol, so for the methane combustion mechanisms considered in this work, only H and H_2 are taken into account. Main flame features printed in Table 2.4 show that the contribution of thermal diffusion (Soret effect) is not very important in these flames. Main important contributions in species discretized equations are due to chemical reactions and ordinary diffusion fluxes, and thermal diffusion has a minor contribution.

2.7 Conclusions

The influence of the level of premixing on the main features of a partially premixed co-flow methane-air laminar flame has been investigated for five levels of premixing from $\Phi = \infty$ (non-premixed flame) to $\Phi = 2.464$. Special emphasis has been given to the pollutant formation (CO and NO_x). In addition, the efficacy/suitability of various existing mathematical sub-models for the solution of these kind of flames has been analysed for both extreme levels of premixing.

Computations have been submitted to a verification procedure to estimate the accuracy of the numerical solutions. This analysis gives an error band where the grid independent solution is expected to be contained (GCI), and also gives a criteria for the mesh selection.

A validation process of the numerical solution for all levels of premixing selected have been carried out observing that a better agreement with the experimental data provided in literature is achieved when the proposed energy boundary condition is employed.

The influence of the level of premixing in the pollutant formation has been studied observing concordance with the results published by other authors. For low Φ, a reduction of NO_x formation is predicted. For the non-premixed flame, CO production does not present a remarkable peak. As the level of premixing increases, the CO peak becomes slender. The CO emission index increases about 10% from $\Phi = 12.32$ to $\Phi = \infty$.

On the prediction of main flame features, there is a certain agreement for all mechanisms employed. However, significant disagreements have been obtained on the estimation of emission indices. When GRI-Mech 2.11 is used, a lower prediction of NO_x is found compared to GRI-Mech 3.0, specially for non-premixed conditions. GRI-Mech 3.0 doubles the NO_x emission with respect to 2.11 release for the non-premixed flame, while for $\Phi = 2.464$ it is 25% higher. While GRI-Mechs predicts a similar amount of CO formation, 42-Step-Mech over-predicts it considerably.

On the transport modelling approaches analysis, the formulation considering non-unity Lewis numbers has been shown to be suitable both in terms of agreement with complex transport and in terms of computational savings. The employment of fixed Lewis numbers means a 25% of CPU time reduction. On the other hand, the consideration of a unity Lewis number notably over-predicts the maximum temperature at the centerline and the flame height. It is also shown that thermal diffusion (Soret effect) has a minor contribution in these kind of flames.

The consideration of radiant heat exchange has been shown to affect the flame temperature considerably and, therefore, the pollutant formation. Thus, a better treatment of this phenomena should to be investigated.

Acknowledgements

This work has been financially supported by the Comisión Interministerial de Ciencia y Tecnología, Spain (project TIC1999-0770), and by the Comissionat per Universitats i Recerca de la Generalitat de Catalunya. Authors also acknowledge the useful suggestions given by Professor Raymond Viskanta.

References

[1] Q.V. Nguyen, R.W. Dibble, C.D. Carter, G.J. Fiechtner, and R.S. Barlow. Raman-LIF measurements of temperature, major species, OH, and NO in a methane-air bunsen flame. *Combustion and Flame*, 105:499–510, 1996.

[2] B.A. Bennett, C.S. McEnally, L.D. Pfefferle, and M.D. Smooke. Computational and experimental study of axissymmetric coflow partially premixed methane/air flames. *Combustion and Flame*, 123:522–546, 2000.

[3] K.H. Lyle, L.K Tseng, J.P Gore, and N.M. Laurendeau. A Study of Pollutant Emission Characteristics of Partially Premixed Turbulent Jet Flames. *Combustion and Flame*, 116:627–639, 1999.

[4] M.D. Smooke, Y. Xu, R.M. Zurn, J.H. Frank, and M.B. Long. Computational and experimental study of OH and CH radicals in axisymmetric laminar diffusion flame. In *Proceedings of the Twenty-Fourth Symposium (International) on Combustion*, pages 813–821, 1992.

[5] M.D. Smooke, C.S. McEnally, and L.D. Pfefferle. Computational and experimental study of soot formation in a coflow, laminar diffusion flame. *Combustion and Flame*, 117:117–139, 1999.

[6] C.S. McEnally and L.D. Pfefferle. Aromatic and linear hydrocarbon concentration measurements in a non-premixed flame. *Combustion Science and Technology*, 116–117:183–209, 1996.

[7] R.E. Mitchell, Sarofim, and L.A. Clomburg. Experimental and numerical investigation of confined laminar diffusion flames. *Combustion and Flame*, 37:227–244, 1980.

[8] V.R. Katta and W.M. Roquemore. Simulation of dynamic methane jet diffusion flames using finite rate chemistry models. *AIAA Journal*, 36(11):2044–2054, 1998.

[9] V.R. Katta, L.P. Goss, and W.M. Roquemore. Effect of nonunity lewis number and finite-rate chemistry on the dynamics of a hydrogen-air jet diffusion flame. *Combustion and Flame*, 96:60–74, 1994.

[10] B.A. Bennett, C.S. McEnally, L.D. Pfefferle, and M.D. Smooke. Local rectangular refinement with application to axisymmetric laminar flames. *Combustion Theory and Modelling*, 2:221–258, 1998.

[11] N. Peters. *Turbulent combustion*. Cambridge University Press, 2000.

[12] J. Cadafalch, C.D. Pérez-Segarra, R. Cònsul, and A. Oliva. Verification of finite volume computations on steady state fluid flow and heat transfer. *Journal of Fluids Engineering*, 124:11–21, 2002.

[13] P.J. Roache. Perspective: a method for uniform reporting of grid refinement studies. *Journal of Fluids Engineering*, 116:405–413, 1994.

[14] R. Cònsul, C.D. Pérez-Segarra, K. Claramunt, J. Cadafalch, and A. Oliva. Detailed numerical simulation of laminar flames by a parallel multiblock algorithm using loosely coupled computers. *Combustion Theory and Modelling*, 7(3):525–544, 2003.

[15] C.S. McEnally and L.D. Pfefferle. Experimental study of nonfuel hydrocarbon concentrations in coflowing partially premixed methane/air flames. *Combustion and Flame*, 118:619–632, 1999.

[16] G.P. Smith, D.M. Golden, M. Frenklach, N.W. Moriarty, B. Eiteneer, M. Goldenberg, C.T. Bowman, R.K. Hanson, S. Song, W.C. Gardiner, V.V. Lissianski, and Z. Qin. Gri-Mech 3.0, http://www.me.berkeley.edu/gri_mech/.

[17] R.B. Bird, E.E. Stewart, and E.N. Lightfoot. *Transport phenomena*. John Wiley and Sons Inc., 1960.

[18] R.J. Kee, F.M. Rupley, and J.A Miller. The Chemkin Thermodynamic Database. Technical report, Sandia National Laboratories, 1987.

[19] R.S. Barlow, A.N. Karpetis, and J.Y. Frank, J.H. Chen. Scalar profiles and NO formation in laminar opposed-flow partially premixed methane/air flames. *Combustion and Flame*, 127:2102–2118, 2001.

[20] S. Mazumder and M.F. Modest. Advanced nongray radiation model coupled with a CFD code for large-scale fire and combustion applications. Technical report, National Sciencie Foundation, 2001.

[21] W.L. Grosshandler. RADCAL: A narrow-band model for radiation calculations in a combustion environment, NIST Technical Note 1402, 1993.

[22] S.R. Marthur and J.Y. Murthy. Pressure boundary conditions for incompressible flow using unstructured meshes. *Numerical Heat Transfer, Part B*, 32:283–298, 1997.

[23] P.H. Gaskell and A.K.C. Lau. Curvature-compensed convective transport: SMART, a new boundedness-preserving transport algorithm. *International Journal for Numerical Methods in Fluids*, 8:617–641, 1988.

[24] S.V. Patankar. *Numerical heat transfer and fluid flow.* Hemiosphere Publishing Corporation, 1980.

[25] B.R. Hutchinson and G.D.Raithby. A multigrid method based on the additive correction strategy. *Numerical Heat Transfer, Part B*, 9:511–537, 1986.

[26] J. Cadafalch, A. Oliva, C.D. Pérez-Segarra, M. Costa, and J. Salom. Comparative study of conservative and nonconservative interpolation schemes for the domain decomposition method on laminar incompressible flows. *Numerical Heat Transfer, Part B*, 35(1):65–84, 1999.

[27] R. Cònsul, C.D. Pérez-Segarra, J. Cadafalch, M. Soria, and A. Oliva. Numerical analysis of laminar flames using the domain decomposition method. In *Proceedings of the Fourth European Computational Fluid Dynamics Conference (ECCOMAS CFD)*, volume 1.2, pages 996–1001, 1998.

[28] J.P. Gore and N.J. Zhan. NO_x emission and major species concentrations in partially premixed laminar methane/air co-flow jet flames. *Combustion and Flame*, 105:414–427, 1996.

[29] T. Takagi and Z. Xu. Numerical analysis of laminar diffusion flames-effects of preferential diffusion of heat and species. *Combustion and Flame*, 96:50–59, 1994.

[30] C.T. Bowman, R.K. Hanson, Davidson, W.C. Gardiner, V.V. Lissianski, G.P. Smith, D.M. Golden, H. Wang, and M. Goldenberg. Gri-Mech 2.11, http://www.me.berkeley.edu/gri_mech/.

[31] M.D. Smooke, R.E. Mitchell, and D.E. Keyes. Numerical solution of two-dimensional axisymmetric laminar diffusion flames. *Combustion Science and Technology*, 67:85–122, 1989.

[32] R.L.G.M. Eggels. *Modelling of Combustion Processes and NO Formation with Reduced Reaction Mechanisms*. PhD thesis, Technical University of Eindhoven, 1996.

[33] M.D. Smooke. Reduced Kinetic Mechanisms and Asymptotic Approximations for Methane-Air Flames. *Lecture Notes in Physics*, 384:1–28, 1991.

[34] N. Peters. Laminar diffusion flamelet models in non-premixed turbulent combustion. *Progress in Energy and Combustion Science*, 10:319–339, 1984.

[35] N. Peters. Laminar flamelet concepts in turbulent combustion. In *Proceedings of the Twenty-First Symposium (International) on Combustion*, pages 1231–1250, 1986.